Tunable Band Gap Photoluminescence from Atomically Thin Transition-Metal Dichalcogenide Alloys

Yanfeng Chen,[†,∥] Jinyang Xi,[‡,∥] Dumitru O. Dumcenco,[§,∥] Zheng Liu,[⊥] Kazu Suenaga,[⊥] Dong Wang,[‡] Zhigang Shuai,[‡] Ying-Sheng Huang,[§] and Liming Xie[†,*]

[†]Key Laboratory of Standardization and Measurement for Nanotechnology of Chinese Academy of Sciences, National Center for Nanoscience and Technology, Beijing 100190, People's Republic of China, [‡]Key Laboratory of Organic Optoelectronics and Molecular Engineering, Department of Chemistry, Tsinghua University, Beijing 100084, People's Republic of China, [§]Department of Electronic Engineering, National Taiwan University of Science and Technology, Taipei 106, Taiwan, Republic of China, and [⊥]Nanotube Research Center, National Institute of Advanced Industrial Science and Technology (AIST), Tsukuba 305-8565, Japan. [∥]These authors contributed equally.

ABSTRACT

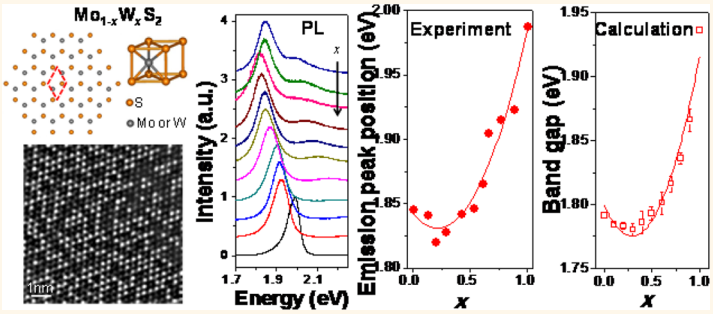

Band gap engineering of atomically thin two-dimensional (2D) materials is the key to their applications in nanoelectronics, optoelectronics, and photonics. Here, for the first time, we demonstrate that in the 2D system, by alloying two materials with different band gaps (MoS_2 and WS_2), tunable band gap can be obtained in the 2D alloys ($Mo_{1-x}W_xS_2$ monolayers, $x = 0-1$). Atomic-resolution scanning transmission electron microscopy has revealed random arrangement of Mo and W atoms in the $Mo_{1-x}W_xS_2$ monolayer alloys. Photoluminescence characterization has shown tunable band gap emission continuously tuned from 1.82 eV (reached at $x = 0.20$) to 1.99 eV (reached at $x = 1$). Further, density functional theory calculations have been carried out to understand the composition-dependent electronic structures of $Mo_{1-x}W_xS_2$ monolayer alloys.

KEYWORDS: two-dimensional material · alloy · transition-metal dichalcogenide · band gap · photoluminescence · density functional theory calculation

Since the discovery of graphene in 2004,[1] atomically thin two-dimensional (2D) materials have attracted broad interest in recent years because of their unique structures, versatile physical properties, and potential applications.[2−8] Toward applications in digital electronics and optoelectronics, sizable and tunable band gap is essential. So far, current 2D materials have limited choices of band gaps (0 eV for graphene, 5.8 eV for hexagonal BN monolayer,[9] 1.9 eV for MoS_2 monolayer,[10,11] 2.1 eV for WS_2 monolayer[12]). Many efforts, such as electrical gating,[13] functionalization,[14] strain,[15] and dielectric screening,[16] have been made to tune the band gap of 2D materials. Still, very limited band gap range has been achieved.

Alloying materials with different band gaps has been widely used in the band gap engineering of bulk semiconductors.[17] Whether alloying can be used to engineer the band gap of 2D materials is still unknown because no atomically thin 2D alloy was obtained. One work on a 2D Ga−Si monolayer bound on a Si(111) substrate showed only localized electronic states but no electronic mixing.[18] However, theoretical calculations have shown that 2D alloys, such as hexagonal BNC monolayer[19,20] and transition-metal dichalcogenide monolayer alloys,[21] could have composition-dependent

* Address correspondence to xielm@nanoctr.cn.

Received for review March 22, 2013 and accepted April 20, 2013.

Published online April 21, 2013
10.1021/nn401420h

band gaps. Therefore, experimental work is needed to assess the electronic structure of 2D alloys.

Experimental effort has been made on BNC alloys. However, BN and graphite are immiscible[22] so that as-synthesized BNC films showed separated BN and graphene domains, and no band gap tuning was observed.[23] The 2D layered transition-metal dichalcogenide alloys may have better intermiscibility and were predicted to be stable.[21] Several layered transition-metal dichalcogenide bulk alloys have been synthesized,[24,25] such as $Mo_{1-x}W_xS_2$ and $Mo_{1-x}W_xSe_2$, suggesting good thermodynamic stability for the corresponding 2D alloys.

Here, we have exfoliated the first family of atomically thin 2D alloys ($Mo_{1-x}W_xS_2$ monolayers) and observed composition-dependent band gap photoluminescence (PL) from the monolayer alloys (1.82 to 1.99 eV). A bowing[26] was observed in the composition-dependent band gap emission of $Mo_{1-x}W_xS_2$ monolayer alloys. Density functional theory (DFT) calculations have shown tunable band gap and band gap bowing for 2D $Mo_{1-x}W_xS_2$ alloys, matching well with experimental results.

RESULTS AND DISCUSSION

Similar to MoS_2 and WS_2,[27] $Mo_{1-x}W_xS_2$ alloy has a layered structure,[28] and each layer consists of two hexagonal S atom layers and a sandwiched Mo/W atom layer. The Mo or W atom sits in the center of a trigonal prismatic cage formed by six S atoms (Figure 1a). The atomic arrangements of Mo and W atoms in monolayer alloys were imaged by scanning transmission electron microscopy (STEM). Figure 1b shows a typical atomic-resolution STEM image of a $Mo_{0.47}W_{0.53}S_2$ monolayer. The W content was determined by energy-dispersive X-ray spectroscopy (EDX) of the bulk crystals (Supporting Information Table S1). Due to its large Z number, the W atom has a larger annular dark-field (ADF) contrast and then is brighter than the Mo atom,[29] which is more clearly seen in the image after fast Fourier transform (FFT) filtering (Figure 1c). Electron energy loss spectroscopy (EELS) characterization on individual atoms further confirmed that the brighter spots, showing two split $O_{2,3}$ EELS peaks at 40−50 eV, were W atoms and the dimer spots, showing one broad $N_{2,3}$ EELS peak at 40−50 eV, were Mo atoms (Figure 1d, EELS of MoS_2 and WS_2 shown in Figure S1).[30] By direct counting of the numbers of Mo and W atoms in STEM images, the W content x can be directly calculated (0.53, with a total of 597 Mo and W atoms counted), consistent with the W content value x of the bulk crystals (0.53, determined by EDX). The arrangements of Mo and W atoms in the monolayer alloy are random (Figure 1b,c), which can be further quantified by a set of short-range order parameters α_i,[31] generally defined by $\alpha_i = 1 - (p_{BA,i}/m_A)$ for AB binary alloys, where $p_{BA,i}$ is the probability that the B atom's ith nearest atom should be A atom (i is an integer), m_A is the atom ratio of A atoms; α_i ranges from $1 - (1/m_A)$ to 1, while 0 generally corresponds to random arrangement of A and B. Analysis of the STEM image (Figure S2) gives α_i values of 0.01, −0.02, −0.03, 0.04 for $i = 1-4$, respectively, revealing random arrangement of Mo and W atoms in the alloy. Systematic STEM imaging and disorder analysis for other $Mo_{1-x}W_xS_2$ monolayer alloys ($0 < x < 1$) showed similar results.[30]

Optical imaging and atomic force microscope (AFM) imaging were used to identify and locate $Mo_{1-x}W_xS_2$ monolayers on Si/SiO_2 substrates (oxide thickness of 300 nm). The $Mo_{1-x}W_xS_2$ monolayers showed a red contrast of 8 to 12% and height of 0.7−1 nm (Figure 2a, b and Figure S3 for $Mo_{0.47}W_{0.53}S_2$, and Figure S4 for other $Mo_{1-x}W_xS_2$ monolayers). The measured height is slightly larger than the interlayer separation (~0.6 nm) in $Mo_{1-x}W_xS_2$ bulk crystals,[32,33] which could be due to adsorbates on the monolayers. Raman and PL mapping showed layer-dependent spectroscopic properties of $Mo_{1-x}W_xS_2$ (Figure 2c−f for $Mo_{0.47}W_{0.53}S_2$ and Figure S5 for other $Mo_{1-x}W_xS_2$ monolayers and bulk materials), which is similar to that observed for MoS_2[10,11] and WS_2.[12,34] Taking $Mo_{0.47}W_{0.53}S_2$ as an example, from bulk to monolayer, the MoS_2-like E^1_{2g} Raman mode[35] at ~383 cm^{-1}, associated with the in-plane vibration of molybdenum and sulfur atoms,[24] upshifted by ~1.5 cm^{-1}. Note that the WS_2-like E^1_{2g} Raman mode at ~350 cm^{-1} (ref 35) is not obvious in $Mo_{0.47}W_{0.53}S_2$ (Figure 2e) but stronger in $Mo_{1-x}W_xS_2$

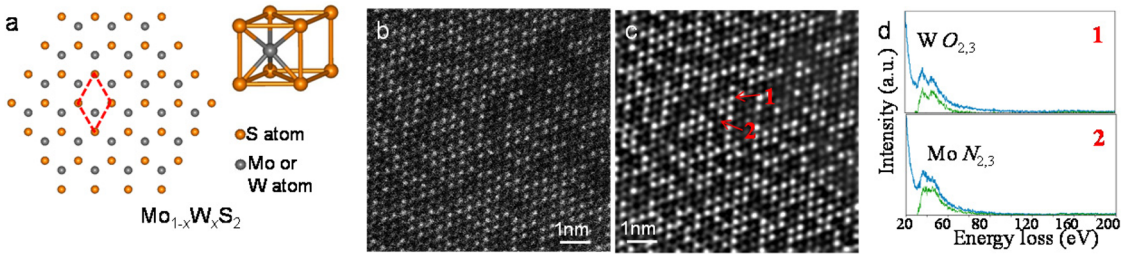

Figure 1. Structure of $Mo_{1-x}W_xS_2$ monolayer. (a) Top view of $Mo_{1-x}W_xS_2$ monolayer and a side view of a unit cell. (b) STEM image of $Mo_{0.47}W_{0.53}S_2$ monolayer. (c) STEM image in panel (b) after FFT filtering, showing two types of atoms with different contrasts. (d) EELS of two individual atoms indicated as "1" and "2" in panel (c), showing EELS characteristics of W (top) and Mo (bottom), respectively. The blue lines are original EELS spectra, and the green lines are spectra after background subtraction.

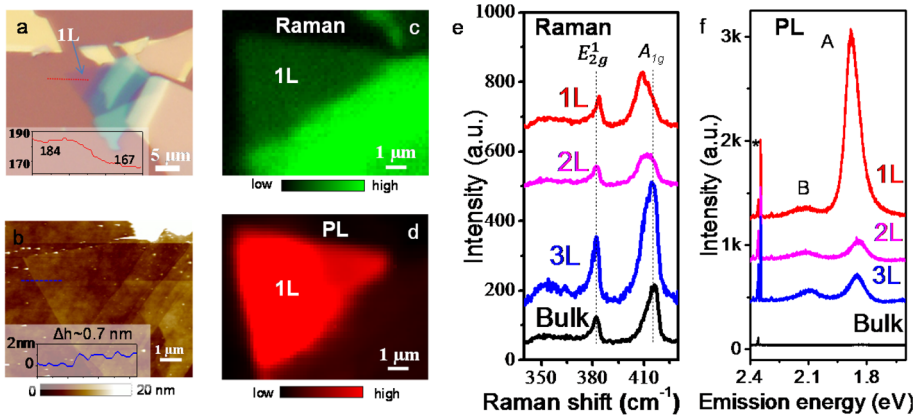

Figure 2. Optical, AFM, Raman, and PL characterizations of $Mo_{0.47}W_{0.53}S_2$ monolayer, few-layers, and bulk. (a) Optical image of exfoliated $Mo_{0.47}W_{0.53}S_2$ flakes on Si/SiO_2 substrate. Monolayer region is labeled as "1L". The inset shows red color intensity along the red dashed line, giving a contrast of (184−167)/184 = 9.2% for the 1L. (b) AFM image of the same $Mo_{0.47}W_{0.53}S_2$ flakes in panel (a). The inset shows the height profile along the blue dashed line. (c) Raman (400−425 cm^{-1}) and (d) PL (1.7−2.25 eV) mapping of the $Mo_{0.47}W_{0.53}S_2$ flakes. (e) Raman and (f) PL spectra of $Mo_{0.47}W_{0.53}S_2$ monolayer (1L), bilayer (2L), trilayer (3L), and bulk samples. Two PL peaks are assigned to A and B excitons.[10] The sharp peaks marked by * in (f) were the Raman peaks from Si substrate and $Mo_{0.47}W_{0.53}S_2$ flakes.

with larger W compositions (Figure S5). The A_{1g} Raman mode at ~416 cm^{-1}, associated with the out-of-plane vibration of sulfur atoms,[24,36] downshifted by ~6 cm^{-1} in monolayer form (Figure 2e). Raman spectra of $Mo_{1-x}W_xS_2$ monolayers with different W composition are shown in Figure S6. Both A_{1g} and E^1_{2g} show two-mode behaviors,[37] in which, from end materials (MoS_2 and WS_2 monolayers) to alloys, MoS_2-like and WS_2-like A_{1g} (E^1_{2g}) shift closer to each other but do not merge. Further work is needed to understand the two-mode behavior for both A_{1g} and E^1_{2g} in $Mo_{1-x}W_xS_2$ monolayers. Note that the WS_2 monolayer showed higher Raman intensity than other $Mo_{1-x}W_xS_2$ monolayers (Figure S6), which is due to resonance effect (laser energy of 2.41 eV, close to B exciton energy of 2.36 eV for WS_2 monolayer).

While no PL emission or weak PL emission was observed for $Mo_{0.47}W_{0.53}S_2$ bulk and few-layers, intense PL emission was observed for the $Mo_{0.47}W_{0.53}S_2$ monolayer (Figure 2d,f). This indicates the transition from an indirect band gap material in its bulk and few-layer forms to a direct band gap semiconductor when thinned to monolayer form. The two PL peaks of $Mo_{0.47}W_{0.53}S_2$ monolayer and few-layers are assigned to the so-called A exciton (low energy one) and B exciton (high energy one) emissions,[28] which are corresponding to band-edge excitonic transitions split by the valence band spin−orbit coupling.[10,11,28]

The band gap of $Mo_{1-x}W_xS_2$ monolayers could be tuned by MoS_2 or WS_2 composition, which was evidenced by PL measurements. As W composition x increases, the A exciton emission (~1.8−2.0 eV) red shifts and then blue shifts (Figure 3a). The B exciton emission (~2.0−2.4 eV) continuously blue shifts (Figure 3b). Figure 3c plots the emission energy against W composition, in which the A exciton emission can be continuously tuned from 1.82 (reached at x = 0.20) to 1.99 eV (reached at x = 1) and the B exciton emission can be tuned from 1.98 (reached at x = 0) to 2.36 eV (reached at x = 1). The valence band spin−orbit coupling changed from 0.14 to 0.37 eV (Figure S7).

The band gap emission energy of $Mo_{1-x}W_xS_2$ monolayers is smaller than the linear combination of that of MoS_2 and WS_2, that is, $E_{PL,Mo_{1-x}W_xS_2} < (1-x)E_{PL,MoS_2} + xE_{PL,WS_2}$, which is the so-called bowing effect as observed in many bulk semiconductor alloys.[17,38] The band gap emission energy bowing of $Mo_{1-x}W_xS_2$ monolayers can be described by

$$E_{PL,Mo_{1-x}W_xS_2} = (1-x)E_{PL,MoS_2} + xE_{PL,WS_2} - bx(1-x) \quad (1)$$

,where b is the so-called bowing parameter. By fitting the experimental data with eq 1, a bowing parameter b of 0.25 ± 0.04 eV can be obtained for A exciton emission (Figure 3c). The B exciton emission also showed a bowing parameter b of 0.19 ± 0.06 eV (Figure 3c). The small difference between bowing parameters for A, B exciton emissions may indicate a weak bowing in composition-dependent valence band spin−orbit coupling. Additionally, the A exciton energy, corresponding to excitonic transition energy at K point, is similar for both $Mo_{1-x}W_xS_2$ monolayers (1.82−1.99 eV) and bulk (1.83−1.95 eV[28]). Considering large exciton binding energy for MoS_2 and WS_2 monolayers (>1 eV),[39,40] the fundamental band gap of $Mo_{1-x}W_xS_2$ monolayers should be much larger than the corresponding direct band−band transition at K point in $Mo_{1-x}W_xS_2$ bulk. This could be due to interaction of an electron (or hole) with the induced surface charge,[41] similar to that in MoS_2 and BN monolayers.[39,42]

To further understand the composition-dependent electronic structure of $Mo_{1-x}W_xS_2$ monolayers, including the origin of the emission energy bowing, DFT calculations were conducted for the monolayer alloys.

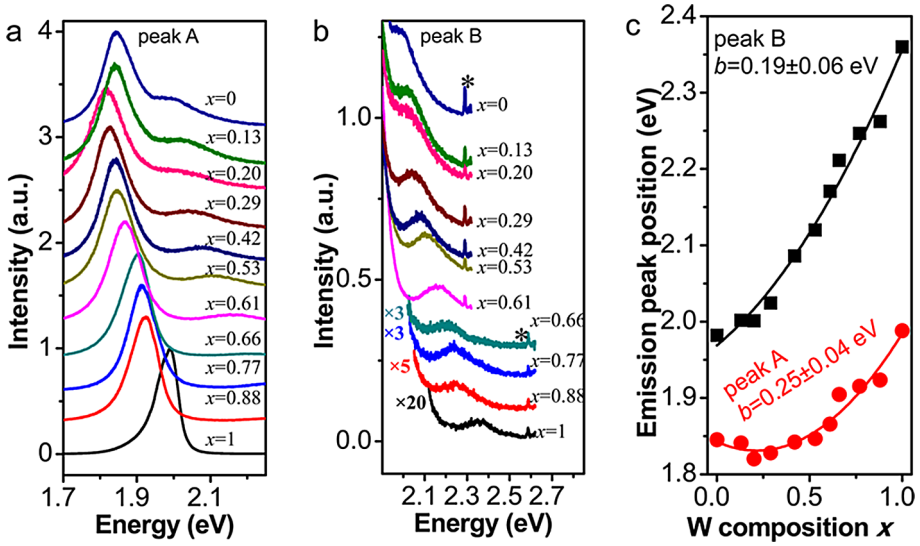

Figure 3. Composition-dependent PL emission from $Mo_{1-x}W_xS_2$ monolayers. (a,b) PL spectra of $Mo_{1-x}W_xS_2$ monolayers with different W compositions *x*. The PL intensity is normalized by the maximum emission intensity (*i.e.*, intensity of A exciton emission at 1.8−2.0 eV). The spectra were excited by 514.5 nm for $x = 0-0.61$ and 457.9 nm for $x = 0.66-1$. The peaks marked by * are Raman peaks of Si substrates. (c) Composition-dependent emission energies for A and B excitons. The red and black lines are parabola fittings for composition-dependent energy of peaks A and B, giving a bowing parameter *b* of 0.25 ± 0.04 and 0.19 ± 0.06 eV, respectively.

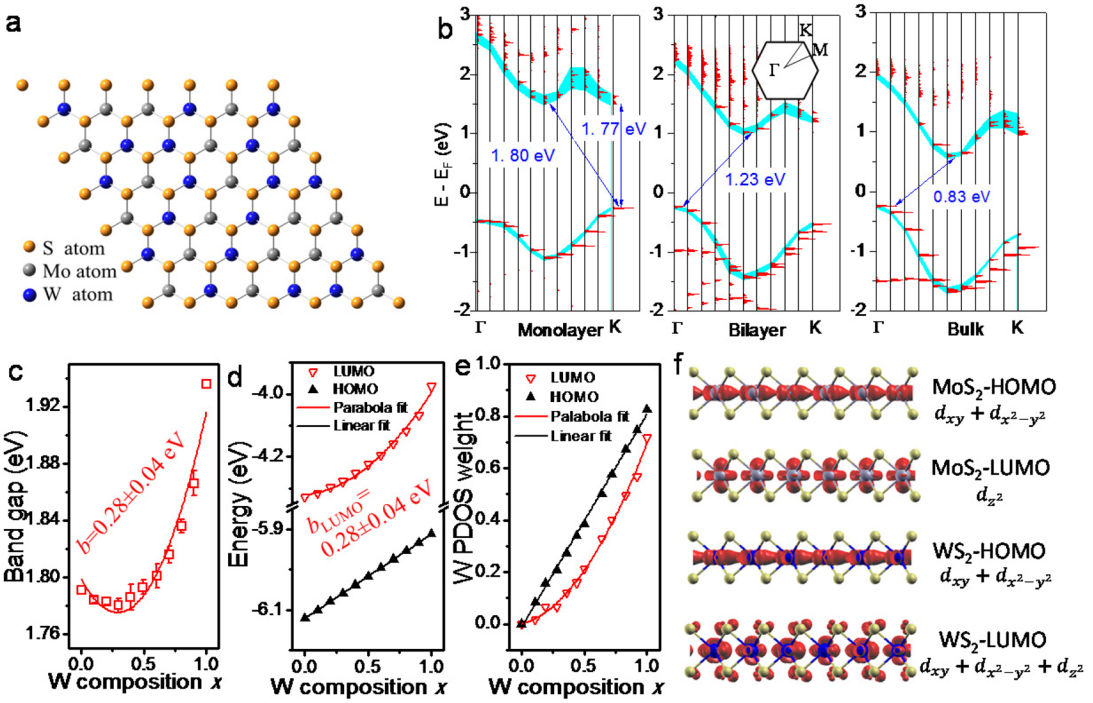

Figure 4. DFT calculations of $Mo_{1-x}W_xS_2$ monolayers. (a) Structure of a 6 × 6 supercell of $Mo_{36-n}W_nS_{72}$ ($n = 18$, corresponding to $Mo_{0.5}W_{0.5}S_2$) in the *a*−*b* plane. (b) EBS of monolayer, bilayer, and bulk materials of $Mo_{0.5}W_{0.5}S_2$. The different $\vec{k}$ vectors in the primitive cell are represented by a thin vertical line. Red areas represent the SFs $A(\vec{k}, E)$ at each $\vec{k}$ point, and the light blue shaded areas represent the SFs' bandwidth for the valence band and conduction band. The primitive cell's first Brillouin zone with three high symmetry points is also shown in the inset. (c) Composition-dependent E_g of $Mo_{1-x}W_xS_2$ monolayers. The error bars represent the standard deviation of E_g calculated from eight different W atom configurations for each W composition *x*. The red line is the parabola fitting, giving a bowing parameter *b* of 0.28 ± 0.04 eV. (d) Energy shift of HOMO and LUMO of $Mo_{1-x}W_xS_2$ monolayers as a function of W composition *x*. Parabola fitting (red line) gives bowing parameter *b* of 0.28 ± 0.04 eV for LUMO. The black line is a linear fit for HOMO shift. (e) Percentage of W projected DOS (PDOS) in HOMO (black triangles) and LUMO (empty red triangles) with different W composition *x*. The red and black lines are parabola and linear fit, respectively. (f) Charge density distribution of HOMO and LUMO for MoS_2 and WS_2 monolayers in the *a*−*c* plane.

In order to model $Mo_{1-x}W_xS_2$ alloys, Mo and W atom configurations were randomly generated (a configuration for $Mo_{0.5}W_{0.5}S_2$ in a 6 × 6 supercell shown in Figure 4a). To analyze the electronic structure of random alloys,

we employed a method[43,44] that transformed the large supercell's eigenstates into an effective band structure (EBS) in the primitive cell. This unfolding procedure can be described by a spectral function (SF) of continuous variable energy E as reported in ref 44. In Figure 4b, the EBS calculations revealed the transition from indirect band gaps for $Mo_{0.5}W_{0.5}S_2$ bulk and bilayer forms to a direct band gap for the monolayer form. Calculations on all $Mo_{1-x}W_xS_2$ monolayers with other W compositions also showed direct band gaps, which is consistent with the observed intense PL emissions from all $Mo_{1-x}W_xS_2$ monolayers.

To model the band gap changes with W composition, eight different configurations for each W composition with larger supercells (9×9) were used in calculations (Figure S8). The average E_g values as well as standard deviations are plotted in Figure 4c as a function of W composition. It is encouraging to find that the trend for band gaps as a function of W composition is very consistent with the experimental data. The band gaps of $Mo_{1-x}W_xS_2$ monolayers first decreased slowly as W composition increased, then a turning point showed up at x around 0.3, after that, the band gaps rose quickly until that of WS_2 was reached. The bowing parameter b is 0.28 ± 0.04 eV by fitting the calculated E_g, matching well with the value from PL experiments (0.25 ± 0.04 eV).

To gain insight into the band gap bowing of $Mo_{1-x}W_xS_2$ monolayer alloys, the highest occupied molecular orbital (HOMO) and the lowest unoccupied molecular orbital (LUMO) positions in $Mo_{1-x}W_xS_2$ monolayers were plotted (Figure 4d and Table S2). A large bowing effect ($b = 0.28 \pm 0.04$ eV) was found for LUMO while there was no bowing for the HOMO. So the band gap bowing of the $Mo_{1-x}W_xS_2$ monolayer alloys originates from bowing of the LUMO energy level. The percentage of W projected density of states (PDOS) in HOMO and LUMO is plotted in Figure 4e as a function of W composition x. It was found that the W PDOS in the HOMO increased linearly with W composition, while that in LUMO exhibited a bowing effect. To understand this, we compared the frontier orbital composition of MoS_2 and WS_2 monolayers. From Figure 4f, it can be seen that the contribution of metal elements to HOMO is identical for MoS_2 and WS_2, both are d_{xy} and $d_{x^2-y^2}$ orbitals. As to LUMO, the major contribution of metal is the d_{z^2} orbital in MoS_2 but d_{xy}, $d_{x^2-y^2}$, and d_{z^2} orbitals in WS_2. Combining Figure 4e,f, we explained the bowing effect of the LUMO as follows: (i) W atoms contributed to the HOMO directly in the alloys due to identical orbital composition for MoS_2 and WS_2, resulting in a linear shift of the HOMO energy level with W composition. (ii) Because of different orbital compositions in the LUMO and higher LUMO energy of WS_2, W atoms contributed less to the LUMO and the energy level shifted up less, and then LUMO bowing occurred. The different contribution of W atoms to the HOMO and LUMO can be clearly seen in the frontier orbital and PDOS analysis (Figure S9 and Table S3).

CONCLUSION

In conclusion, a series of transition-metal dichalcogenide monolayer alloys ($Mo_{1-x}W_xS_2$, $x = 0$ to 1 with a step of ~0.1) have been cleaved from their bulk crystals. STEM imaging showed random distribution nature of the Mo and W atom arrangements in $Mo_{1-x}W_xS_2$ monolayer alloys. Both PL experiments and DFT simulations showed that the band gap of $Mo_{1-x}W_xS_2$ monolayers can be tuned by changing the W composition. The band gap of $Mo_{1-x}W_xS_2$ monolayers showed a large bowing effect, attributed to different LUMO compositions of MoS_2 and WS_2 and then LUMO bowing in $Mo_{1-x}W_xS_2$. The realization of band gap tuning in atomically thin 2D alloys and various choices of layered transition-metal dichalcogenides with minimal lattice mismatch but versatile electronic properties[5,45] could allow wide-range band gap tuning and then burst applications of 2D materials in nanoelectronics and optoelectronics.

METHODS

Sample Preparation. $Mo_{1-x}W_xS_2$ single crystals were grown by the chemical vapor transport method described in refs 24 and 28. X-ray analysis confirmed 2H-type structure for all $Mo_{1-x}W_xS_2$ single crystals. $Mo_{1-x}W_xS_2$ monolayer and few-layer samples were mechanically exfoliated on Si/SiO_2 (300 nm SiO_2) substrates from bulk $Mo_{1-x}W_xS_2$ single crystals using a similar technique as employed for graphene.[1]

Characterization. The location, shape, and layer number of $Mo_{1-x}W_xS_2$ flakes were determined by combination of optical contrast and atomic force microscopy (AFM) imaging (Figure S3 and Figure S4). Optical images were taken on an Olympus BX51 microscope using a 100× objective. Red contrast is defined by $(I_{R,substrate} - I_{R,sample})/I_{R,substrate}$, where $I_{R,substrate}$ is the red channel intensity on the substrate and $I_{R,sample}$ is the red channel intensity on the sample. Tapping mode AFM was done on a Veeco IIIa or a DI 3100 multimode microscope.

The exfoliated monolayers were transferred onto transmission electron microscope (TEM) microgrids for STEM-EELS characterizations. A JEOL 2100F TEM with the DELTA corrector was operated at 60 kV for STEM-EELS experiments, which carries 20 pA current within 0.1 nm probe. GIF Quantum was used for spectroscopy. The convergence angle for the incident probe was set to 30 mrad, while the EELS collection angle was around 45−60 mrad. The acquisition time for each spectrum is typically 0.01 s. FFT filtering of STEM images was conducted in ImageJ.

Raman and PL measurements were done on a JY Horiba HR800 micro-Raman spectroscope under ambient conditions at room temperature. The laser power was ~0.4 mW for 514.5 nm excitation and ~0.2 mW for 457.9 nm excitation; 1800 and 600 lines/mm gratings were used in Raman and PL measurements, respectively. Lorentzian peak function was used in Raman peak fitting, and Gaussian peak function was used in PL peak fitting.

DFT Calculation. Band structure calculations of $Mo_{1-x}W_xS_2$ monolayers were performed with the real-space projector-augmented wave method[46] in the local density approximation[47]

as implemented in the Vienna ab initio simulation package (VASP).[48] The experimental structure of the bulk MoS_2, which has a lattice constant of 3.1602 Å,[27] was used in first principles calculations. The energy convergence criteria for the electronic self-consistent cycle was set to 10^{-5} eV, and an energy cutoff of 400 eV was used for plane waves throughout our calculations. In order to model the full band structure of $Mo_{1-x}W_xS_2$ monolayer alloys, we built a supercell of $3 \times 36 = 108$ atoms, which is made up of 6×6 primitive cells. In the band structure calculation of $Mo_{0.5}W_{0.5}S_2$ bilayer and bulk in Figure 4b, supercells with two $Mo_{0.5}W_{0.5}S_2$ layers on the *c*-axis were used. The procedure of unfolding large supercell's eigenstates into an effective band structure (EBS) in the primitive cell was described by a spectral function (SF) of continuous variable energy *E*:[44]

$$A(\vec{k}, E) = \Sigma_{m,n} |\langle \vec{K}m|\vec{k}n\rangle|^2 \delta(E_m - E) \quad (2)$$

where the $|\vec{k}n\rangle$ and $|\vec{K}m\rangle$ (*n* and *m* are for band indices) are the Bloch states in the primitive cell and supercell, respectively. In particular, the different local environments in the alloy will be reflected in a finite width of $A(\vec{k},E)$ in both arguments $\vec{k}$ and *E*. With the supercell determined for a set of $\{\vec{k}\}$ and over a wide range of energies, we can obtain the alloy EBS.

For calculation of the composition-dependent band gap of $Mo_{1-x}W_xS_2$ monolayer alloys, a supercell made up of 9×9 primitive cells was used. For a given composition of W, eight configurations were generated by randomly distributing W atoms in the supercell in substitution of Mo atoms. Owing to the two-dimensional structure of the monolayer $Mo_{1-x}W_xS_2$, vacuum energy level was obtained along the lattice *c*-axis by the electrostatic potential calculation (Figure S10), which is similar to the approach used to derive work function in the thin slab calculation.[49,50]

Conflict of Interest: The authors declare no competing financial interest.

Acknowledgment. Y.C. and L.X. acknowledge China 973 program (2011CB932803). J.X., D.W., and Z.S. are supported by National Natural Science Foundation of China (21273124, 21290191). D.D. and Y.H. acknowledge the support of the National Science Council of Taiwan under Project Nos. NSC 100-2112-M-011-001-MY3 and NSC 101-2811-M-011-002. Z.L. and K.S. acknowledge the support of the JST research acceleration program.

Supporting Information Available: EDX characterization of $Mo_{1-x}W_xS_2$ single crystals, EELS of MoS_2 and WS_2, calculation of short-range order parameters from STEM images, optical, AFM, Raman and PL characterizations of $Mo_{1-x}W_xS_2$ monolayers and bulk, composition-dependent splitting of A and B emissions, supercells with different W configurations for each W compositions *x*, table of composition-dependent HOMO, LUMO, and E_g, composition-dependent charge density distributions of HOMO and LUMO, vacuum energy level calibration, PDOS analysis of HOMO and LUMO for each W compositions *x*. This material is available free of charge *via* the Internet at http://pubs.acs.org.

REFERENCES AND NOTES

1. Novoselov, K. S.; Geim, A. K.; Morozov, S. V.; Jiang, D.; Zhang, Y.; Dubonos, S. V.; Grigorieva, I. V.; Firsov, A. A. Electric Field Effect in Atomically Thin Carbon Films. *Science* **2004**, *306*, 666–669.
2. Wang, H.; Yu, L.; Lee, Y.-H.; Shi, Y.; Hsu, A.; Chin, M. L.; Li, L.-J.; Dubey, M.; Kong, J.; Palacios, T. Integrated Circuits Based on Bilayer MoS_2 Transistors. *Nano Lett.* **2012**, *12*, 4674–4680.
3. Xia, F. N.; Farmer, D. B.; Lin, Y. M.; Avouris, P. Graphene Field-Effect Transistors with High On/Off Current Ratio and Large Transport Band Gap at Room Temperature. *Nano Lett.* **2010**, *10*, 715–718.
4. Radisavljevic, B.; Radenovic, A.; Brivio, J.; Giacometti, V.; Kis, A. Single-Layer MoS_2 Transistors. *Nat. Nanotechnol.* **2011**, *6*, 147–150.
5. Wang, Q. H.; Kalantar-Zadeh, K.; Kis, A.; Coleman, J. N.; Strano, M. S. Electronics and Optoelectronics of Two-Dimensional Transition Metal Dichalcogenides. *Nat. Nanotechnol.* **2012**, *7*, 699–712.
6. Xia, F. N.; Mueller, T.; Lin, Y. M.; Valdes-Garcia, A.; Avouris, P. Ultrafast Graphene Photodetector. *Nat. Nanotechnol.* **2009**, *4*, 839–843.
7. Reina, A.; Jia, X. T.; Ho, J.; Nezich, D.; Son, H. B.; Bulovic, V.; Dresselhaus, M. S.; Kong, J. Large Area, Few-Layer Graphene Films on Arbitrary Substrates by Chemical Vapor Deposition. *Nano Lett.* **2009**, *9*, 30–35.
8. Lin, Y. M.; Valdes-Garcia, A.; Han, S. J.; Farmer, D. B.; Meric, I.; Sun, Y. N.; Wu, Y. Q.; Dimitrakopoulos, C.; Grill, A.; Avouris, P.; *et al.* Wafer-Scale Graphene Integrated Circuit. *Science* **2011**, *332*, 1294–1297.
9. Tarrio, C.; Schnatterly, S. E. Interband-Transitions, Plasmons, and Dispersion in Hexagonal Boron-Nitride. *Phys. Rev. B* **1989**, *40*, 7852–7859.
10. Mak, K. F.; Lee, C.; Hone, J.; Shan, J.; Heinz, T. F. Atomically Thin MoS_2: A New Direct-Gap Semiconductor. *Phys. Rev. Lett.* **2010**, *105*, 136805.
11. Splendiani, A.; Sun, L.; Zhang, Y. B.; Li, T. S.; Kim, J.; Chim, C. Y.; Galli, G.; Wang, F. Emerging Photoluminescence in Monolayer MoS_2. *Nano Lett.* **2010**, *10*, 1271–1275.
12. Gutierrez, H. R.; Perea-Lopez, N.; Elias, A. L.; Berkdemir, A.; Wang, B.; Lv, R.; Lopez-Urias, F.; Crespi, V. H.; Terrones, H.; Terrones, M. Extraordinary Room-Temperature Photoluminescence in WS_2 Triangular Monolayers. *Nano Lett.* **2012**, 10.1021/nl3026357.
13. Zhang, Y. B.; Tang, T. T.; Girit, C.; Hao, Z.; Martin, M. C.; Zettl, A.; Crommie, M. F.; Shen, Y. R.; Wang, F. Direct Observation of a Widely Tunable Bandgap in Bilayer Graphene. *Nature* **2009**, *459*, 820–823.
14. Balog, R.; Jorgensen, B.; Nilsson, L.; Andersen, M.; Rienks, E.; Bianchi, M.; Fanetti, M.; Laegsgaard, E.; Baraldi, A.; Lizzit, S.; *et al.* Bandgap Opening in Graphene Induced by Patterned Hydrogen Adsorption. *Nat. Mater.* **2010**, *9*, 315–319.
15. Scalise, E.; Houssa, M.; Pourtois, G.; Afanas'ev, V. V.; Stesmans, A. Strain-Induced Semiconductor to Metal Transition in the Two-Dimensional Honeycomb Structure of MoS_2. *Nano Res.* **2012**, *5*, 43–48.
16. Mao, N. N.; Chen, Y. F.; Liu, D. M.; Zhang, J.; Xie, L. M. Solvatochromic Effect on Photoluminescence of MoS_2 Monolayer. *Small* **2013**, 10.1002/smll.201202982.
17. Adachi, S. *Properties of Semiconductor Alloys: Group-IV, III-V and II-VI Semiconductors*; Wiley: Chichester, U.K., 2009.
18. Ebert, P.; Landrock, S.; Jiang, Y.; Wu, K. H.; Wang, E. G.; Dunin-Borkowski, R. E. Electronically Nonalloyed State of a Statistical Single Atomic Layer Semiconductor Alloy. *Nano Lett.* **2012**, *12*, 5845–5849.
19. Peng, Q.; De, S. Tunable Band Gaps of Mono-layer Hexagonal Bnc Heterostructures. *Physica E* **2012**, *44*, 1662–1666.
20. Lam, K. T.; Lu, Y. H.; Feng, Y. P.; Liang, G. C. Stability and Electronic Structure of Two Dimensional $C_x(BN)_y$ Compound. *Appl. Phys. Lett.* **2011**, *98*, 022101.
21. Komsa, H.-P.; Krasheninnikov, A. V. Two-Dimensional Transition Metal Dichalcogenide Alloys: Stability and Electronic Properties. *J. Phys. Chem. Lett.* **2012**, *3*, 3652–3656.
22. Tomashik, V. In *Refractory Metal Systems*; Effenberg, G., Ilyenko, S., Eds.; Springer: Berlin, 2009; Vol. 11E1, pp 444−473.
23. Ci, L.; Song, L.; Jin, C. H.; Jariwala, D.; Wu, D. X.; Li, Y. J.; Srivastava, A.; Wang, Z. F.; Storr, K.; Balicas, L.; *et al.* Atomic Layers of Hybridized Boron Nitride and Graphene Domains. *Nat. Mater.* **2010**, *9*, 430–435.
24. Dumcenco, D. O.; Chen, K. Y.; Wang, Y. P.; Huang, Y. S.; Tiong, K. K. Raman Study of 2H-$Mo_{1-x}W_xS_2$ Layered Mixed Crystals. *J. Alloys Compd.* **2010**, *506*, 940–943.
25. Yousefi, G. H.; Agarwal, M. K. Hall-Effect Measurements of $Mo_{1-x}W_xSe_2$ ($0 \leq x \leq 1$) Dichalcogenide Single-Crystals. *J. Mater. Sci. Lett.* **1993**, *12*, 1731–1732.
26. Vanvecht, J. A.; Bergstre, T. K. Electronic Structures of Semiconductor Alloys. *Phys. Rev. B* **1970**, *1*, 3351–3358.
27. Podberezskaya, N. V.; Magarill, S. A.; Pervukhina, N. V.; Borisov, S. V. Crystal Chemistry of Dichalcogenides MX_2. *J. Struct. Chem.* **2001**, *42*, 654–681.

28. Ho, C. H.; Wu, C. S.; Huang, Y. S.; Liao, P. C.; Tiong, K. K. Temperature Dependence of Energies and Broadening Parameters of the Band-Edge Excitons of $Mo_{1-x}W_xS_2$ Single Crystals. *J. Phys.: Condens. Matter* **1998**, *10*, 9317–9328.
29. Krivanek, O. L.; Chisholm, M. F.; Nicolosi, V.; Pennycook, T. J.; Corbin, G. J.; Dellby, N.; Murfitt, M. F.; Own, C. S.; Szilagyi, Z. S.; Oxley, M. P.; *et al.* Atom-by-Atom Structural and Chemical Analysis by Annular Dark-Field Electron Microscopy. *Nature* **2010**, *464*, 571–574.
30. Dumcenco, D. O.; Kobayashi, H.; Liu, Z.; Huang, Y. S.; Suenaga, K. Visualization and Quantification of Transition Metal Atomic Mixing in $Mo_{1-x}W_xS_2$ Single Layers. *Nat. Commun.* **2012**, *4*, 1351.
31. Cowley, J. M. Short-Range and Long-Range Order Parameters in Disordered Solid Solutions. *Phys. Rev.* **1960**, *120*, 1648–1657.
32. Thomazeau, C.; Geantet, C.; Lacroix, M.; Danot, M.; Harle, V. EXAFS Characterization of New Active Phases for Catalytic Hydrotreatment: Two Cations Disulfide Layers in the $Mo_xW_{(1-x)}S_2$ Lamellar Solid Solution. *Oil Gas Sci. Technol.* **2005**, *60*, 781–790.
33. Thomazeau, C.; Geantet, C.; Lacroix, M.; Harle, V.; Benazeth, S.; Marhic, C.; Danot, M. Two Cation Disulfide Layers in the $W_xMo_{(1-x)}S_2$ Lamellar Solid Solution. *J. Solid State Chem.* **2001**, *160*, 147–155.
34. Ding, Y.; Wang, Y. L.; Ni, J.; Shi, L.; Shi, S. Q.; Tang, W. H. First Principles Study of Structural, Vibrational and Electronic Properties of Graphene-like MX_2 (M = Mo, Nb, W, Ta; X = S, Se, Te) Monolayers. *Physica B* **2011**, *406*, 2254–2260.
35. Dumcenco, D. O.; Su, Y. C.; Wang, Y. P.; Chen, K. Y.; Huang, Y. S.; Ho, C. H.; Tiong, K. K. Polarization Dependent Raman Active Modes Study of the $Mo_{1-x}W_xS_2$ Mixed Layered Crystals. *Chin. J. Phys.* **2011**, *49*, 270–277.
36. Lee, C.; Yan, H.; Brus, L. E.; Heinz, T. F.; Hone, J.; Ryu, S. Anomalous Lattice Vibrations of Single- and Few-Layer MoS_2. *ACS Nano* **2010**, *4*, 2695–2700.
37. Chang, I. F.; Mitra, S. S. Application of a Modified Random-Element-Isodisplacement Model to Long-Wavelength Optic Phonons of Mixed Crystals. *Phys. Rev.* **1968**, *172*, 924–933.
38. Yin, W. J.; Gong, X. G.; Wei, S. H. Origin of the Unusually Large Band-Gap Bowing and the Breakdown of the Band-Edge Distribution Rule in the Sn_xGe_{1-x} Alloys. *Phys. Rev. B* **2008**, *78*, 161203.
39. Komsa, H. P.; Krasheninnikov, A. V. Effects of Confinement and Environment on the Electronic Structure and Exciton Binding Energy of MoS_2 from First Principles. *Phys. Rev. B* **2012**, *86*, 241201.
40. Ramasubramaniam, A. Large Excitonic Effects in Monolayers of Molybdenum and Tungsten Dichalcogenides. *Phys. Rev. B* **2012**, *86*, 115409.
41. Delerue, C.; Allan, G.; Lannoo, M. Dimensionality-Dependent Self-Energy Corrections and Exchange-Correlation Potential in Semiconductor Nanostructures. *Phys. Rev. Lett.* **2003**, *90*, 076803.
42. Wirtz, L.; Marini, A.; Rubio, A. Excitons in Boron Nitride Nanotubes: Dimensionality Effects. *Phys. Rev. Lett.* **2006**, *96*, 126104.
43. Popescu, V.; Zunger, A. Effective Band Structure of Random Alloys. *Phys. Rev. Lett.* **2010**, *104*, 236403.
44. Popescu, V.; Zunger, A. Extracting *E versus* $\vec{k}$ Effective Band Structure from Supercell Calculations on Alloys and Impurities. *Phys. Rev. B* **2012**, *85*, 085201.
45. Wilson, J. A.; Yoffe, A. D. The Transition Metal Dichalcogenides Discussion and Interpretation of the Observed Optical, Electrical and Structural Properties. *Adv. Phys.* **1969**, *18*, 193–335.
46. Kresse, G.; Joubert, D. From Ultrasoft Pseudopotentials to the Projector Augmented-Wave Method. *Phys. Rev. B* **1999**, *59*, 1758–1775.
47. Kohn, W.; Sham, L. J. Self-Consistent Equations Including Exchange and Correlation Effects. *Phys. Rev.* **1965**, *140*, A1133–A1138.
48. Kresse, G.; Furthmuller, J. Efficient Iterative Schemes for *Ab Initio* Total-Energy Calculations Using a Plane-Wave Basis Set. *Phys. Rev. B* **1996**, *54*, 11169–11186.
49. Sgiarovello, C.; Binggeli, N.; Baldereschi, A. Influence of Surface Morphology on the Si(100) and (111) Ionization Potentials. *Phys. Rev. B* **2001**, *64*, 195305.
50. Fall, C. J.; Binggeli, N.; Baldereschi, A. Deriving Accurate Work Functions from Thin-Slab Calculations. *J. Phys.: Condens. Matter* **1999**, *11*, 2689–2696.